ACS Catalysis

pubs.acs.org/acscatalysis Research Article

Effect of Chemically Distinct Substrates on the Mechanism and Reactivity of a Highly Promiscuous Metallohydrolase

Gaurav Sharma, Vindi M. Jayasinghe-Arachchige, Qiaoyu Hu, Gerhard Schenk, and Rajeev Prabhakar*

Cite This: ACS Catal. 2020, 10, 3684−3696 Read Online

ACCESS | Metrics & More | Article Recommendations | Supporting Information

ABSTRACT: In this DFT study, the substrate promiscuity of the binuclear [Fe(II)-Zn(II)] core containing glycerophosphodiesterase (GpdQ) from *Enterobacter aerogenes* has been investigated through the hydrolysis of three chemically diverse groups of substrates: i.e., phosphomono-, phosphodi-, and phosphotriesters. The hydrolysis of these substrates is studied by comparing stepwise, concerted, and substrate-assisted mechanisms. Both the stepwise and concerted mechanisms occur with similar barriers, while the energetics for the substrate-assisted mechanism are significantly less favorable. Irrespective of the mechanism, active site residue His217 plays a critical role, in agreement with structural, kinetics, and spectroscopic data, but the transition state of the reaction depends on the identity of the substrate (dissociative for the triester paraoxon, associative for the monoester 4-nitrophenyl phosphate (NPP), and in-between for the diesters glycerol-3-phosphoethanolamine (GPE) and bis(4-nitrophenyl)phosphate (BNPP)). In good agreement with available kinetic and spectrophotometric data, the calculations highlight the preference of GpdQ for diester substrates, followed by tri- and monoesters. For substrates with two different types of scissile bonds (paraoxon and GPE) a clear preference for the bond with the stronger electron withdrawing leaving group was observed. The extensive agreement between experimental data and DFT calculations enhances the understanding of the mechanism of GpdQ-catalyzed hydrolysis and paves the way for the rational design of optimized catalysts for the hydrolysis of different types of phosphoesters.

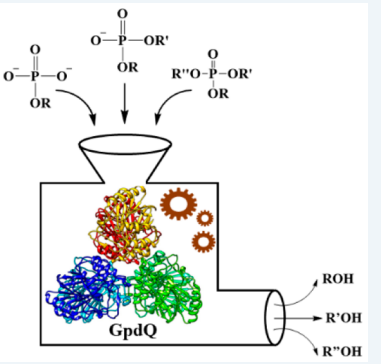

KEYWORDS: *phosphoester hydrolysis, glycerophosphodiesterase (GpdQ), metallohydrolase, substrate promiscuity, reaction mechanisms and density functional theory (DFT)*

1. INTRODUCTION

Glycerophosphodiesterase (GpdQ) from *Enterobacter aerogenes*[1,2] is a member of the family of binuclear metallohydrolases that are commonly found in bacteria, yeast, plants, and mammals. Enzymes from this family include aminopeptidases, lactamases, nucleases, protein phosphatases, purple acid phosphatases (PAPs), and ureases, and they have been implicated in several critical biological processes such as DNA replication, bone turnover, iron transport, and the generation of reactive oxygen species (ROS).[3−11] Among the metallohydrolases, phosphatases form a subgroup that catalyzes the hydrolysis of a range of phosphoester bonds.[7−9] In general, there are three types of phosphoester bonds (i.e., mono-, di-, and triesters) that are hydrolyzed by specialized enzymes known as phosphomono-, phosphodi-, and phosphotriesterases, respectively. GpdQ exhibits extensive substrate promiscuity, while diesters such as glycerol-3-phosphoethanolamine (GPE) are its preferred and biologically most relevant substrates.[1,2] This enzyme also hydrolyzes a range of non-natural phosphomono-, phosphodi-, and phosphotriester substrates such as 4-nitrophenyl phosphate (NPP), bis(4-nitrophenyl) phosphate (BNPP), and diethyl 4-nitrophenyl-phosphate (paraoxon) over a large pH range (Figure 1a).[1,2,12−15] Since the substrates of this enzyme include several organophosphate pesticides and nerve agents such as paraoxon, demeton, sarin, soman, and VX, it has considerable potential in agricultural remediation and as an antiwarfare agent.[14−17]

GpdQ possesses remarkable coordination flexibility, also known as "breathing of the active site cleft", whereby the interaction with a substrate molecule alters the coordination environment of one of the two catalytically essential metal ions in the active site. Specifically, ligand Asn80 in the β site dissociates upon substrate binding (Figure 1b).[13,18] This type of flexibility has also been reported for other metalloenzymes, including soybean lipoxygenase[19,20] and *E. coli* DNA polymerase I.[7,21] In GpdQ the coordination flexibility exhibited by the metal−Asn80 bond dissociation not only optimizes the catalytic efficiency of this enzyme but also may contribute to its substrate promiscuity.[13,22]

The X-ray structures of Co(II)- and Fe(II)-substituted GpdQ have been solved at 1.9 Å (PDB ID: 3D03)[18] and 2.2 Å

Received: November 8, 2019
Revised: February 20, 2020
Published: February 24, 2020

https://dx.doi.org/10.1021/acscatal.9b04847
ACS Catal. 2020, 10, 3684−3696

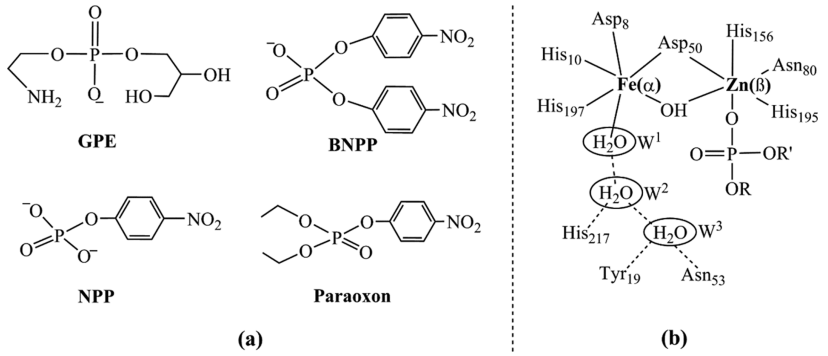

Figure 1. (a) Chemical structures of the substrates GPE, BNPP, paraoxon, and NPP. (b) Active site of GpdQ.

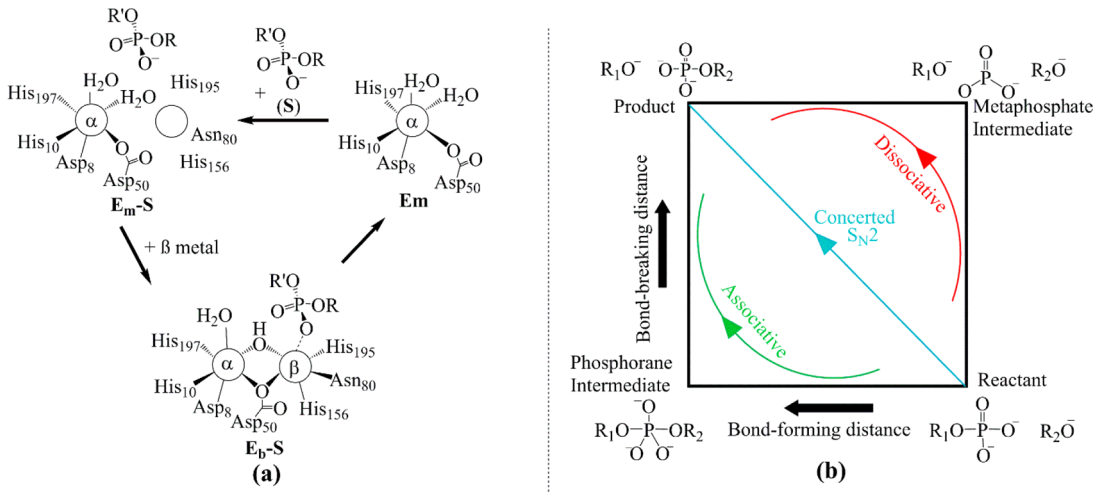

Figure 2. (a) Proposed mechanism for the formation of the binuclear metal center of GpdQ. (b) General mechanisms for phosphoester hydrolysis.

(PDB ID: 2ZO9) resolution, respectively.[23] While the overall folds of these two structures are very similar, only in the Co(II)-containing structure are a terminal, α-metal-bound water and two additional water molecules that are integrated into a hydrogen-bond network with Tyr19, Asn53, and His217 residues observed (in good agreement with the MCD data; Figure S1). Overall, the GpdQ polypeptide is structurally similar to other α/β sandwich phosphoesterases such as PAPs and Mre11 nuclease.[24,25] GpdQ is a homohexameric enzyme with each subunit containing binding sites for two closely spaced metal ions (α and β sites) in the catalytic center.[23,26] The α metal ion coordinates to Asp8, His10, and His197 and the β metal to Asn80, His156, and His195 (Figure 1b).[23] The two metal ions are bridged through the Asp50 residue and a hydroxyl molecule (μ-OH). This ligand environment is identical with that of the cyclic phosphodiesterase Rv0805[27] from *Mycobacterium tuberculosis* and very similar to that of PAPs (with the His10 → Tyr substitution being the only difference),[7,24,25] methionine aminopeptidase,[10,28] and metallo-β-lactamases.[11,25] Atomic absorption spectroscopy and anomalous scattering measurements indicate that Fe(II) is likely to occupy the α metal ion binding site in the catalytic center (Figure 1b).[23] However, the *in vivo* composition of the metal ions of GpdQ remains unknown.[23] Metal ion substitution experiments have shown that the enzyme exhibits *in vitro* activity in the presence of both homobinuclear and heterobinuclear compositions of divalent metal ions such as Fe(II), Zn(II), Cd(II), Mn(II), and Co(II).[12,22,23,29] Other binuclear metallohydrolases, in particular the organophosphate pesticide degrading phosphotriesterases[24] (e.g., the phosphotriesterase from *Pseudomonas diminuta* (PTE)[30] or the organophosphate-degrading hydrolase from *Agrobacterium radiobacter* (OpdA))[31] have a similar promiscuous use of metal ions, while others are more restricted (e.g., the Ni(II)-dependent ureases,[32] the Mn(II)-dependent arginases,[33] or Fe(III)-M(II)-dependent purple acid phosphatases (where M = Fe, Zn, Mn)).[34]

According to the mechanism proposed by a combination of solid-state structural data, spectroscopic studies (mainly magnetic circular dichroism), site-directed mutagenesis, and the measurement of kinetic isotope effects,[13,23,35−37] GpdQ is catalytically inactive and mononuclear in the resting state ($\mathbf{E_m}$ in Figure 2a; the metal is bound to the α site); the addition of a substrate (S) triggers a rapid conformational change (rate ~350 s^{-1}) in the active site that enhances the affinity of the β site for a metal ion ($\mathbf{E_m}$-**S** complex). The subsequent binding of the second metal (rate ~40 s^{-1}) then activates the enzyme ($\mathbf{E_b}$-**S** complex; Figure 2a).[13] It takes approximately another 1 min for the enzyme to reach its optimal catalytic efficiency in a process that is linked to the aforementioned coordination flexibility.[13] The process of $\mathbf{E_b}$-**S** formation is independent of the identity of the metal ions or substrates.[13] After the creation of the active $\mathbf{E_b}$-**S** species, the hydrolysis of the substrate is initiated through a nucleophilic attack by a deprotonated, metal ion bound water molecule. While PAPs and some organophosphate-degrading hydrolases (i.e., OpdA) can use hydroxides that are coordinated either in a terminal position to only one metal ion or in a metal-bridging mode (depending on

https://dx.doi.org/10.1021/acscatal.9b04847
ACS Catal. 2020, 10, 3684−3696

experimental conditions),[38,39] GpdQ strictly relies on a terminally coordinated hydroxide (located in the α site) to initiate hydrolysis.[40]

Three distinct mechanisms are possible for the metallohydrolase-catalyzed reactions with phosphate esters, illustrated in the More O'Ferrall−Jencks diagram (Figure 2b).[41] (1) In the $D_N + A_N$ model, a dissociative or elimination−addition mechanism proceeds via a trigonal metaphosphate intermediate. In this mechanistic model, the detachment of the leaving group, R_1O, precedes the formation of a new bond between the nucleophile (R_2OH) and the phosphate entity (denoted by a red line in Figure 2b). (2) In the D_NA_N model, a dissociative associative mechanism, also called synchronous, takes place through the simultaneous formation and cleavage of the phosphoester bonds. In this mechanism, a concerted process (analogous to S_N2 substitution) leads to the final product (represented by a blue line in Figure 2b). (3) In the $A_N + D_N$ model, an associative mechanism, also termed as an addition−elimination mechanism, proceeds via a pentavalent phosphorane intermediate. Here, there is no significant cleavage of the P−OR_1 bond (leaving group) during the formation of a new P−OR_2 (nucleophile) bond (represented by a green line in Figure 2b). It has been suggested that hydrolysis of phosphomono-, phosphodi-, and phosphotriester substrates employ either the concerted D_NA_N or associative ($A_N + D_N$) mechanism; a completely dissociative mechanism has not yet been observed for any of those substrate types.[42,43] The tightness of the transition state in these mechanisms, described in terms of the P−O(nucleophile) and P−O(leaving group) bond distances, decreases from mono- to triesters (Figure 2b).[44] Members of the binuclear metallohydrolase family have been proposed to employ a different mechanism depending on the nature of the substrate.[30,42,43,45−58]

Despite a considerable amount of experimental data,[13,18,36,59] the precise molecular details of the mechanism employed by GpdQ, including the contributions from the metal ions and residues of the second coordination sphere and the nature of its transition states, remain subject to debate. It is also unknown how (or if) the identity of the substrate affects the mechanism. In order to address these gaps in knowledge, we employed a DFT-based approach to investigate the reaction mechanism with four chemically distinct substrates (NPP, BNPP, GPE, and paraoxon) that represent all three types of phosphoesters. The results of this study provide insight into factors that guide the substrate selectivity of GpdQ and may be of relevance to metallohydrolases in general, providing guidance for the design of catalysts with tailored properties for diverse applications.

2. COMPUTATIONAL DETAILS

2.1. Modeling. The model of the active site of GpdQ was constructed using the 1.9 Å X-ray crystal structure of the free enzyme with Co(II) ions in the α and β sites (PDB ID: 3D03).[18] Since anomalous scattering data indicated that Fe(II) and Zn(II) are the most likely metal ions in the α and β sites in vivo, respectively,[23] the Co(II) ions in the crystal structure were substituted accordingly. The model used in the computations thus includes the binuclear [Fe(Asp8, His10, Asp50, His197)-Zn(Asp50, Asn80, His156, His195)] metal center and all key second coordination shell residues (Tyr19, Asn53, His 81, and His217; Figure 1b). These residues are proposed to be involved in the positioning of the substrate at the active site and the stabilization of transition states.[13] In order to retain the strain of the surrounding protein environment on the active site, the backbone C atoms of all amino acids in the model were kept fixed to their positions from the X-ray structure (Figure S2). In the active site model, aspartates were modeled as an acetate, histidines as 4-methyl-1*H*-imidazole, asparagine as acetamide, and tyrosine as 4-methylphenol. Furthermore, a metal-bridging hydroxide (μ-OH), a water molecule bound to the α metal ion (and that is deprotonated to the hydrolysis-initiating nucleophile during the reaction[13]), and two additional active site water molecules observed in the X-ray structure were included (Figure S2). The models of all enzyme−substrate (E-S) complexes were built by utilizing the equilibrated structures provided by our previous 100 ns molecular dynamics (MD) simulations using two different force fields, AMBER[60] and AMOEBA[61,62] (see the Supporting Information for details).[63] The initial structures of the substrates NPP, GPE, BNPP, and paraoxon for the simulations were taken from their crystal structures[64] and optimized in the gas phase using the Gaussian09 program at the MPW1PW91/Lanl2dz[65] level of theory. These simulations accurately predicted the experimentally proposed roles of the first and second coordination shell residues in substrate binding and coordination flexibility of the active site.[13] The MD-derived structures were truncated to build the different conformations of the E-S models. These models were subsequently optimized at the MPW1PW91/Lanl2dz level.[65] The lowest energy structures (Figures S3 and S8−S10) provided by these calculations were used as the reactants to investigate reaction mechanisms. Each of the GpdQ−substrate complexes exist in the singlet ground state, with both the triplet and quintet states being substantially higher in energy. The enzyme−substrate models contain different numbers of atoms and charges for diverse substrates: i.e., atoms = 166 and charge = −1 for GPE, atoms = 171 and charge = −1 for BNPP, atoms = 172 and charge = 0 for paraoxon, and atoms = 158 and charge = −2 for NPP.

2.2. Computational Procedure. All calculations were performed using the Gaussian 09 program package.[66] The geometry optimizations of reactants, intermediates, transition states, and products were carried out at the MPW1PW91/Lanl2dz level[65] using the corresponding Hay−Wadt effective core potential[67] for Fe and Zn. Hessians were also calculated at the same level of theory as the optimizations to confirm the nature of the stationary points along the reaction coordinates. The transition states were confirmed to have only one negative eigenvalue corresponding to the reaction coordinates. Intrinsic reaction coordinate (IRC) scans were performed to ascertain the existence of all minima and maxima on the same potential energy surface (PES). The effects of the surrounding protein environment were computed using a dielectric constant of 4.3, corresponding to diethyl ether, and utilizing the self-consistent reaction field (SCRF) integral equation formalism polarizable continuum model (IEFPCM) method[68] at the MPW1PW91[65]/Lanl2dz level. The final energies of the optimized structures were further improved by performing single-point calculations including additional d and p polarization functions for oxygen (β = 0.96), nitrogen (β = 0.74), carbon (β = 0.59), hydrogen (β = 0.36), and phosphorus (β = 0.36), respectively (obtained from the EMSL's Gaussian basis set library).[69] The Gibbs free energies obtained at the MPW1PW91/[Lanl2dz+d(P,O,N,C)+p(H)] level, including zero-point vibrational energies, thermal corrections and solvent effects in the protein, were computed. The natural bonding

https://dx.doi.org/10.1021/acscatal.9b04847
ACS Catal. 2020, 10, 3684−3696

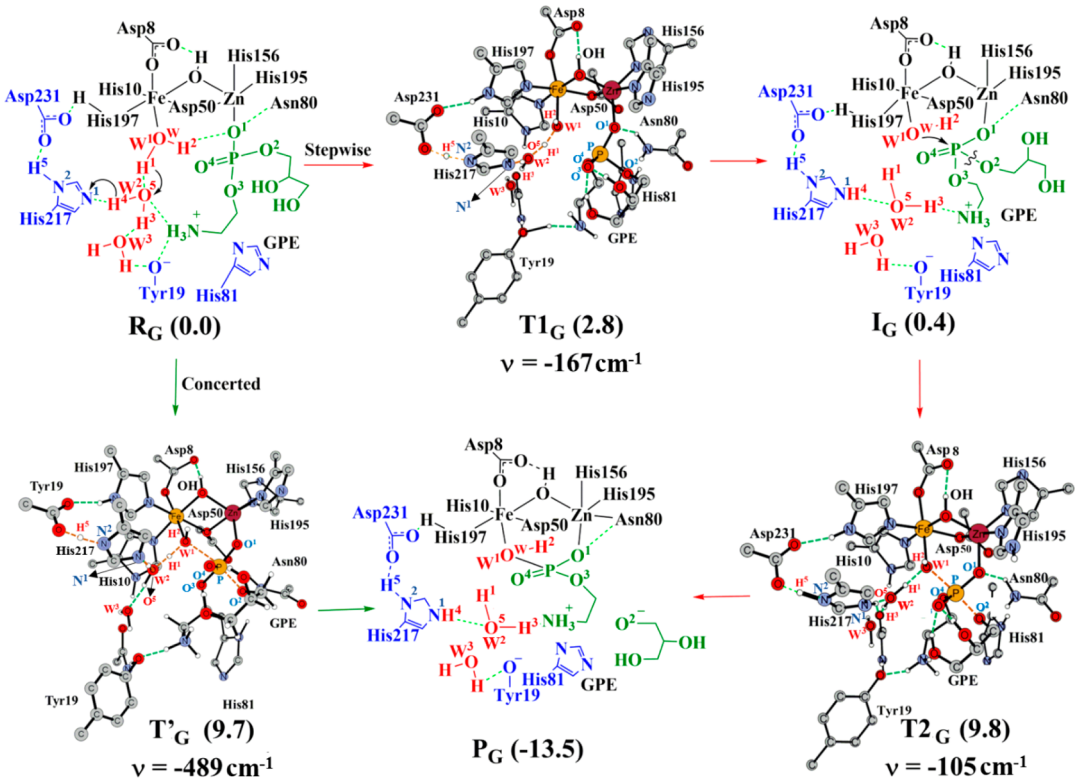

Figure 3. Structures (Å) and energies (kcal/mol) of the stepwise (red arrows) and the concerted (green arrows) mechanisms for the GPE hydrolysis.

orbital (NBO) charges and electrostatic surface potentials (ESPs) of all four isolated substrates were computed in the gas phase at the MPW1PW91/Lanl2dz level.

To determine the effects of other DFT functionals and basis sets on the energetics, the rate-limiting barriers for the reactions with the substrates GPE and NPP were computed with four functionals (MPW1PW9, M06-2X,[70] B3LYP,[71,72] and PBE1PBE[73]) using the [Lanl2dz+d(P,O,N,C)+p(H)] basis set. In comparison to the MPW1PW91 functional, all of these functionals slightly increase the barrier by 1−3 kcal/mol. The barriers computed using the basis sets DGDZVP[74] and SDD[75] for all atoms are also found to be lower by ∼2 kcal/mol using the MPW1PW91 functional for the GpdQ-NPP and GpdQ-GPE complexes. The deviations in the energetics of these reactions were less than 3 kcal/mol, thus demonstrating that the overall outcome of our study and its interpretation are not dependent on the methodology. Additionally, the inclusion of dispersion effects, utilizing Grimme's function with the Becke−Johnson damping effect (GD3BJ)[76] using the MPW1PW91 functional,[65] reduces the barriers by 1−2 kcal/mol for the GpdQ-NPP and GpdQ-GPE complexes.

3. RESULTS AND DISCUSSION

In this study, catalytic mechanisms of GpdQ using four distinct substrates, i.e. NPP (a phosphomonoester), GPE and BNPP (both phosphodiesters), and paraoxon (a phosphotriester), have been investigated. These substrates vary significantly in regard to relevant chemical properties such as size, charge, and electrostatic surface potential, as well as the length and nature of the scissile P−O bonds (Figure S4).

3.1. Mechanism of GPE Hydrolysis. GPE, a natural phosphodiester substrate of GpdQ, contains two different leaving groups, glycerolate and aminoethanolate (Figure 1a). Their presence facilitates several hydrogen-bonding interactions in the active site of the enzyme, including those with the μ-OH and three water molecules (Figure 3). The binding of a large substrate such as GPE is aided by coordination flexibility (i.e., the dissociation of ligand Asn80 from the metal in the β site; note that Asn80 maintains a hydrogen bond with the glycerolate leaving group of the substrate). In the GpdQ-GPE complex, the metal ions are still bridged by Asp50 and μ-OH, and the aminoethanolate leaving group forms a hydrogen bond with Tyr19 (Figure 3). The μ-OH group is located opposite from the substrate. An analysis of alternative conformations (Figure S3) indicates that the one shown in Figure 3 is the most stable arrangement. In the Fe(N_2O_4)-Zn(N_2O_3) metal center of the catalytically competent enzyme−substrate complex, the coordination numbers of the α and β sites are 6 and 5, respectively (Figure 3), in agreement with experimental data.[13,22,25] Following the formation of this complex, hydrolysis of the ester bond(s) is initiated by a terminally coordinated hydroxide.[40] Here, we investigated the cleavage of both the glycerolate ($P-O^2$) and aminoethanolate ($P-O^3$) ester groups using three alternative mechanisms termed stepwise, concerted, and substrate-assisted. Among them, the last mechanism requires the assistance of the substrate ("substrate-assisted mechanism"; Figure S5). The barrier for the hydrolysis of GPE in this mechanism was found to be prohibitively high (32.2 kcal/mol; details are provided in the Supporting Information). Therefore, this mechanism was not further explored for other substrates.

3.1.1. Stepwise Mechanism. In the reactant ($\mathbf{R_G}$ in Figure 3), GPE is coordinated to the Zn(II) ion in the β site in a monodentate fashion and the W^1 water is bound to the Fe(II) ion in the α site. In this structure, the aminoethanolate leaving group is in a position *trans* to W^1. Due to the Lewis acidity of

https://dx.doi.org/10.1021/acscatal.9b04847
ACS Catal. 2020, 10, 3684−3696

Table 1. Key Geometrical Bond Distances (Å) and NBO Charges (e) of the Optimized Structures for the Stepwise and Concerted Mechanisms of the GPE Hydrolysis

	bond distance (Å)									NBO charge (e)		
	O^W–H^1	H^1–O^5	O^5–H^4	H^4–N^1	Fe–O^W	Zn–O^1	Fe–Zn	P–O^2	P–O^W	Fe	P	O^W
Stepwise Mechanism												
$\mathbf{R}_G$	0.99	1.88	1.05	1.60	2.01	2.07	3.08	1.71	3.61	0.55	2.54	−0.91
$\mathbf{T1}_G$	1.24	1.31	1.21	1.22	2.02	2.06	3.07	1.71	3.72	0.57	2.48	−0.92
$\mathbf{I}_G$	2.31	1.01	2.10	1.02	2.03	2.03	3.07	1.72	3.79	0.60	2.45	−0.93
$\mathbf{T2}_G$	2.52	0.98	1.46	1.09	2.10	1.99	3.02	1.97	2.22	0.59	2.43	−0.95
$\mathbf{P}_G$	5.82	1.03	2.03	0.99	2.08	2.04	3.03	4.06	1.72	0.56	2.56	−0.97
Concerted Mechanism												
$\mathbf{T'}_G$	1.21	1.22	1.11	1.40	2.12	1.99	3.02	1.96	2.20	0.57	2.53	−0.94

the metal, the scissile P–O^2 bond (1.71 Å) of GPE in $\mathbf{R}_G$ becomes elongated by 0.09 Å in comparison to its free form. Linked to this observed elongation is an increase in the electrophilicity of the P atom of GPE (its charge increases by 0.17e; Table 1 and Figure S4). The Fe–Zn, Fe–O^W, and Zn–O^1 bond distances in $\mathbf{R}_G$ are 3.08, 2.01, and 2.07 Å, respectively. Not only does W^1 coordinate with Fe(II) via its oxygen atom (O^W) but it also forms hydrogen bonds with W^2 and GPE. These combined interactions are expected to lower its pK_a value significantly[77,78] and are commonly utilized to activate a nucleophile in metallohydrolases (including *E. coli* alkaline phosphatase[56] and OpdA[46]). For GpdQ the pK_a of this water molecule has been estimated from kinetic measurements to be ∼9.5.[13] Furthermore, the hydrogen-bonding network formed by water molecules W^1–W^2–W^3 stabilizes the negative charge on the phosphoryl center of GPE. Thus, the first step of the (stepwise) mechanism involves the formation of the nucleophilic, Fe(II)-bound hydroxide moiety. This process is aided by the three hydrogen-bonded water molecules, with residue His217 likely being the base and ultimate acceptor of the proton from W^1 (Figure 3). In principle, residues His81 and Tyr19 could also act as a base in this initial step. This suggestion is supported by the observed activity of the His217Ala mutant.[12] However, in comparison to His217 the relative energy barriers for the concerted mechanism discussed below are increased by 7.3 and 12.4 kcal/mol, respectively. Furthermore, a histidine residue corresponding to His217 with a similar proposed role as a base is present in PAP,[79] RNaseZ,[80] and phosphoprotein phosphatases.[81] In GpdQ this initial step occurs with a small barrier of 2.8 kcal/mol (see transition state $\mathbf{T1}_G$ in Figure 3). All key distances in this optimized transition state support the concerted nature of this process (Table 1). In the intermediate formed in this process ($\mathbf{I}_G$), the positive charge on the His217 base is stabilized by the negatively charged Asp231. The removal of Asp231 in the model significantly increases the barrier for this step by 8.2 kcal/mol. A similar role of the His-Asp dyad has been proposed for thermolysin.[82] As a result of this easy proton transfer, this step is almost thermoneutral: i.e., the energy difference between $\mathbf{R}_G$ and $\mathbf{I}_G$ is only 0.4 kcal/mol.

In the next step of the (stepwise) mechanism, the Fe-bound O^WH^2 nucleophile attacks the electrophilic P atom of the Zn(II)-coordinated GPE, triggering the cleavage of the P–O^2 bond (Figure 3). In the optimized transition state ($\mathbf{T2}_G$), all key distances confirm the synchronized nature of this step (P–O^2 = 1.97 Å and P–O^W = 2.22 Å). The sum of the P–O^W(nucleophile) and P–O^2(leaving group) distances illustrate the progression of the hydrolytic step; a comparison between these distances in $\mathbf{I}_G$ and $\mathbf{T2}_G$ indicates a significant increase in tightness from 5.51 Å to 4.19 Å. The barrier for this step is 9.8 kcal/mol, making it the rate-limiting step of the entire reaction. The product state ($\mathbf{P}_G$), including the separated glycerolate leaving group, is exergonic by 13.5 kcal/mol in comparison to $\mathbf{R}_G$. In this state, the monoester derivative of GPE remains bound to the active site.

3.1.2. Concerted Mechanisms. The creation of the O^WH^2 nucleophile and its attack on the electrophilic P atom could also occur in a single step (see $\mathbf{I''}_G$ in Figure S6 and Table S1).[83,84] It is noteworthy that these processes take place in two different steps through intermediate $\mathbf{I}_G$ in the previous stepwise mechanism (Figure 3). This concerted step incurs a 20.1 kcal/mol barrier, which is 10.3 kcal/mol higher than the rate-limiting step in the stepwise mechanism discussed above and which is reflected in an elongated P–O^W distance (+0.09 Å) and shortened Fe–O^W distance (−0.06 Å) in the optimized transition state $\mathbf{T1''}_G$ for this single-step process. Additionally, the barrier of 31.8 kcal/mol for the cleavage of the P–O^2 bond in this mechanism is prohibitively high.

In an alternative concerted mechanistic model, the $\mathbf{I}_G$ intermediate is bypassed altogether and all of the steps discussed in the stepwise mechanism (section 3.1.1) occur in a single step (Figure 3). According to this mechanism, the deprotonation/activation of the Fe(II)-bound W^1, its attack of the P atom, and the cleavage of the P–O^2 bond occur in a concerted manner. The associated energy barrier is 9.7 kcal/mol, virtually identical with the rate-limiting transformation of $\mathbf{I}_G$ to $\mathbf{P}_G$ in the stepwise model (9.8 kcal/mol). Furthermore, the bond distances that are indicative of the progress of the ester cleavage (i.e., P–O^2 and P–O^W) are very similar in these two models (Table 1), with their sum being slightly smaller in the concerted model (4.19 Å vs 4.16 Å).

Since the barriers for the stepwise and concerted mechanisms are nearly indistinguishable, only the latter model was used to compute the energetics for the hydrolysis of the second phosphoester bond of GPE. In the reactant ($\mathbf{R}_{GA}$), the aminoethanolate group is in a position *trans* to the W^1 nucleophile (Figure S7 and Table S2). From $\mathbf{R}_{GA}$, via the transition state ($\mathbf{T}_{GA}$) the cleavage of the P–O^3 bond occurs with a barrier of 14.4 kcal/mol, which is 4.7 kcal/mol higher than the barrier computed for the cleavage of the glycerolate leaving group (Figure 3). This difference is likely to be due to the lower stabilization of $\mathbf{T}_{GA}$ (five hydrogen bonds) in comparison to $\mathbf{T'}_G$ (seven hydrogen bonds) by the reorganization of the active site and distinct binding modes of the substrate. The hydrogen bonds in the latter are also stronger than those in $\mathbf{T}_{GA}$. Additionally, the P atom is more electrophilic in $\mathbf{T'}_G$, possessing a 0.10e greater charge than in $\mathbf{T}_{GA}$. Furthermore, the P–O^2 bond in $\mathbf{T'}_G$ is more activated

https://dx.doi.org/10.1021/acscatal.9b04847
ACS Catal. 2020, 10, 3684−3696

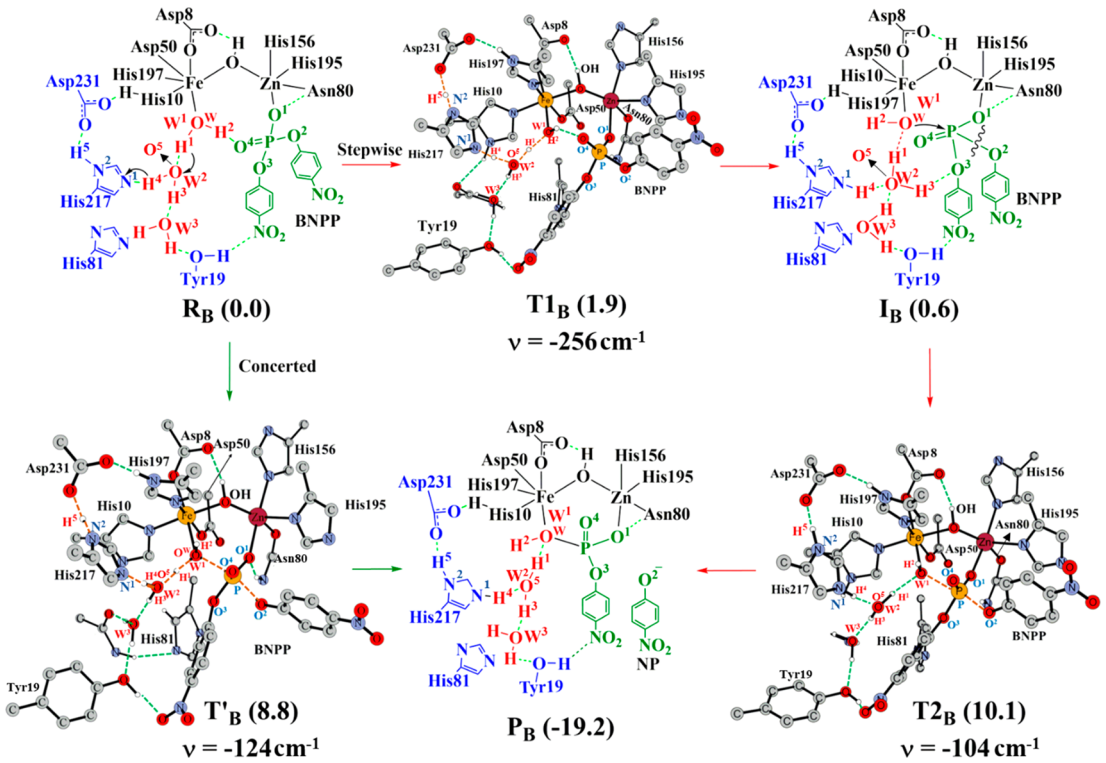

Figure 4. Structures (Å) and energies (kcal/mol) of the stepwise (red arrows) and concerted (green arrows) mechanisms for the BNPP hydrolysis.

Table 2. Key Geometrical Bond Distances (Å) and NBO Charges (e) of the Optimized Structures for the Stepwise and Concerted Mechanisms of the BNPP Hydrolysis

	bond distance (Å)									NBO charge (e)		
	O^W–H^1	H^1–O^5	O^5–H^4	H^4–N^1	Fe–O^W	Zn–O^1	Fe–Zn	P–O^2	P–O^W	Fe	P	O^W
Stepwise Mechanism												
$\mathbf{R_B}$	1.02	1.62	1.02	1.66	2.06	2.16	3.56	1.76	3.03	0.61	2.52	−0.93
$\mathbf{T1_B}$	1.21	1.32	1.27	1.21	2.05	2.15	3.55	1.79	3.03	0.60	2.47	−0.96
$\mathbf{I_B}$	2.54	1.00	2.12	1.01	2.04	2.16	3.55	1.78	3.02	0.60	2.47	−0.97
$\mathbf{T2_B}$	2.39	1.01	2.31	1.02	2.20	1.92	3.61	1.98	2.06	0.63	2.50	−0.95
$\mathbf{P_B}$	1.26	1.04	1.56	1.07	2.05	2.08	3.54	3.34	1.64	0.58	2.57	−1.04
Concerted Mechanism												
$\mathbf{T'_B}$	1.24	1.28	1.19	1.20	2.21	2.11	3.61	1.96	2.05	0.64	2.47	−0.94

than the P–O^3 bond in $\mathbf{T_{GA}}$ from the corresponding reactants (i.e., it is shorter by 0.20 Å; Table 1 and Table S2). The final product ($\mathbf{P_{GA}}$) is 1.0 kcal/mol less exergonic than $\mathbf{P_G}$: i.e., 12.5 kcal/mol lower in energy from $\mathbf{R_{GA}}$. All of these factors are likely to be responsible for a clear preference for the cleavage of the P–O^2 over the P–O^3 bond.

In summary, our calculations support a crucial role of His217 as a base in the hydrolysis of GPE. While the energy profile does not allow a distinction between the stepwise and concerted mechanisms, the calculations demonstrate that the cleavage of the glycerolate (P–O^2) bond of GPE is energetically more favorable than hydrolysis of the amino-ethanolate (P–O^3) bond.

3.2. Mechanism of BNPP Hydrolysis. BNPP is also a phosphodiester, but in contrast to GPE, it contains two identical leaving groups: i.e., two *p*-nitrophenolates (Figure 1a). In the most stable GpdQ-BNPP complex, one of the nitrophenyl groups directly interacts with the active site, while the second group is exposed to the solvent (Figure 4).[63] BNPP interacts with multiple second coordination shell residues (i.e. His81, Gln166, Met167, and Ile170) of the enzyme and the conserved water molecule (W^1) coordinated to Fe(II) through both CH–π and hydrogen-bonding interactions.[35,63] In contrast to the GpdQ-GPE complex, in the GpdQ-BNPP complex (i.e., reactant $\mathbf{R_B}$) the metal ions are bridged only via a hydroxide group (μ-OH); Asp50 is coordinated only to Fe(II). As a result, the Fe–Zn distance in $\mathbf{R_B}$ is substantially longer (by 0.48 Å) than that in $\mathbf{R_G}$ (Table 2). The bond lengths between Zn(II) and the monodentately coordinated substrate (Zn–O^1) and Fe(II) and W^1 (Fe–O^W) are also longer by 0.09 and 0.05 Å, respectively, in $\mathbf{R_B}$ (Table 2). Upon binding to the active site, the scissile P–O^2 bond of BNPP is elongated by 0.10 Å.

3.2.1. Stepwise Mechanism. As already observed in the stepwise reaction with GPE, the transition from $\mathbf{R_B}$ to $\mathbf{I_B}$ (via the transition state $\mathbf{T1_B}$) involves a proton transfer from the Fe(II)-bound water molecule (W^1) to His217 (Figures 3 and 4). This process is again almost thermoneutral (+0.6 kcal/mol) and has an even lower barrier than the corresponding reaction with GPE (1.9 kcal/mol vs 2.8 kcal/mol for the optimized

https://dx.doi.org/10.1021/acscatal.9b04847
ACS Catal. 2020, 10, 3684−3696

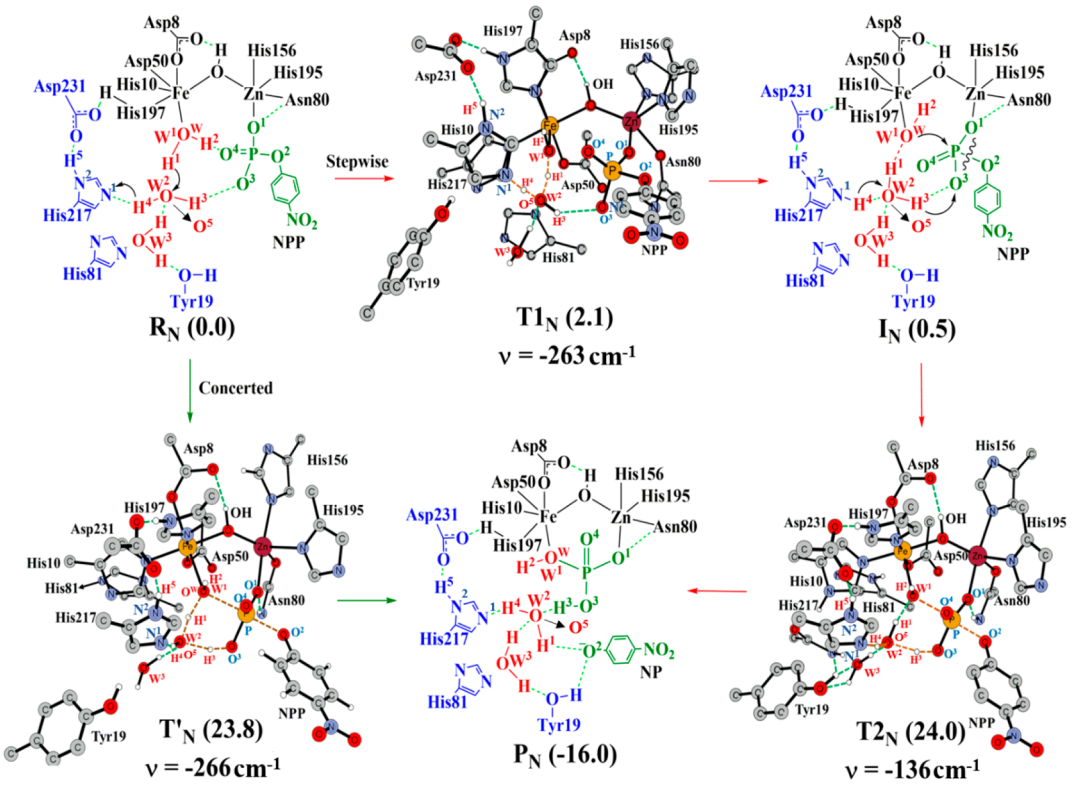

Figure 5. Structures (Å) and energies (kcal/mol) of the stepwise (red arrows) and concerted (green arrows) mechanisms for the NPP hydrolysis.

Table 3. Key Geometrical Bond Distances (Å) and NBO Charges (e) of the Optimized Structures for the Stepwise and Concerted Mechanisms of the NPP Hydrolysis

	bond distance (Å)									NBO charge (e)		
	O^W-H^1	H^1-O^5	O^5-H^4	H^4-N^1	$Fe-O^W$	$Zn-O^1$	Fe–Zn	$P-O^2$	$P-O^W$	Fe	P	O^W
Stepwise Mechanism												
$\mathbf{R_N}$	0.99	3.61	1.01	1.72	1.97	2.15	3.61	1.83	3.03	0.56	2.45	−0.89
$\mathbf{T1_N}$	1.23	1.38	1.24	1.28	2.00	2.15	3.60	1.84	3.63	0.58	2.42	−0.98
$\mathbf{I_N}$	2.34	1.06	2.30	1.01	1.93	2.14	3.63	1.84	3.12	0.54	2.43	−0.96
$\mathbf{T2_N}$	2.21	1.03	1.15	1.21	2.09	2.08	3.67	1.99	2.23	0.56	2.43	−0.98
$\mathbf{P_N}$	3.06	1.01	1.06	1.50	2.06	2.10	3.54	6.06	1.74	0.58	2.53	−0.96
Concerted Mechanism												
$\mathbf{T'_N}$	1.33	1.13	1.02	1.67	2.18	2.05	3.64	1.96	2.21	0.56	2.43	−0.98

transition states $\mathbf{T1_B}$ and $\mathbf{T1_G}$, respectively). In intermediate $\mathbf{I_B}$ both $P-O^2$ and $Zn-O^1$ bonds are longer than the corresponding bonds in $\mathbf{I_G}$ (Tables 1 and 2).

In the next step, the nucleophilic attack by the Fe-bound O^WH^2 group cleaves the $P-O^2$ bond. The barrier for this rate-determining step (10.1 kcal/mol) is almost identical with that of the reaction with GPE (9.8 kcal/mol), but the transition state is significantly tighter: i.e., more associative (the respective sums of the $P-O^W$ and $P-O^2$ distances are 4.19 and 4.04 Å; Tables 1 and 2). The product state $\mathbf{P_B}$ is considerably more exergonic than its counterpart formed in the reaction with GPE (−19.2 kcal/mol vs −13.5 kcal/mol), largely due to the presence of a hydrogen bond between O^W and W^2 (Figure 4).

3.2.2. Concerted Mechanism. As discussed for the reaction with GPE, the formation of the nucleophile and its attack on the phosphorus atom may also occur in a concerted, simultaneous step, thus bypassing the intermediate $\mathbf{I_B}$ (Figure 4). The energy barrier for this mechanism is again approximately 1 kcal/mol smaller than that for the corresponding reaction with GPE, and the transition is negligibly more associative (by 0.03 Å) than in the stepwise mechanism.

Due to their similar energetics, it is not possible to determine which mechanism is more likely; both are equally plausible. In the product state ($\mathbf{P_B}$) a nitrophenolate group is released and the monoester product, i.e. NPP, remains bound to the active site in a μ-1,3-metal ion bridging mode. Its hydrolysis will be discussed below.

3.3. Mechanism of NPP Hydrolysis. NPP is the monoester formed upon the hydrolysis of BNPP (see above and Figure 1a). Due to the presence of three nonesterified phosphate oxygens, NPP contains the highest electronegative charge among all four substrates. The charge distribution and electrostatic surface potential show that this charge is localized on the phosphate group (Figure S4). In the GpdQ-NPP complex, the substrate binds monodentately to Zn(II) and its nitrophenyl group is located on the opposite side of W^1, thus being exposed to the solvent. Consequently, the leaving group does not form any contacts with active site residues, similar to

https://dx.doi.org/10.1021/acscatal.9b04847
ACS Catal. 2020, 10, 3684−3696

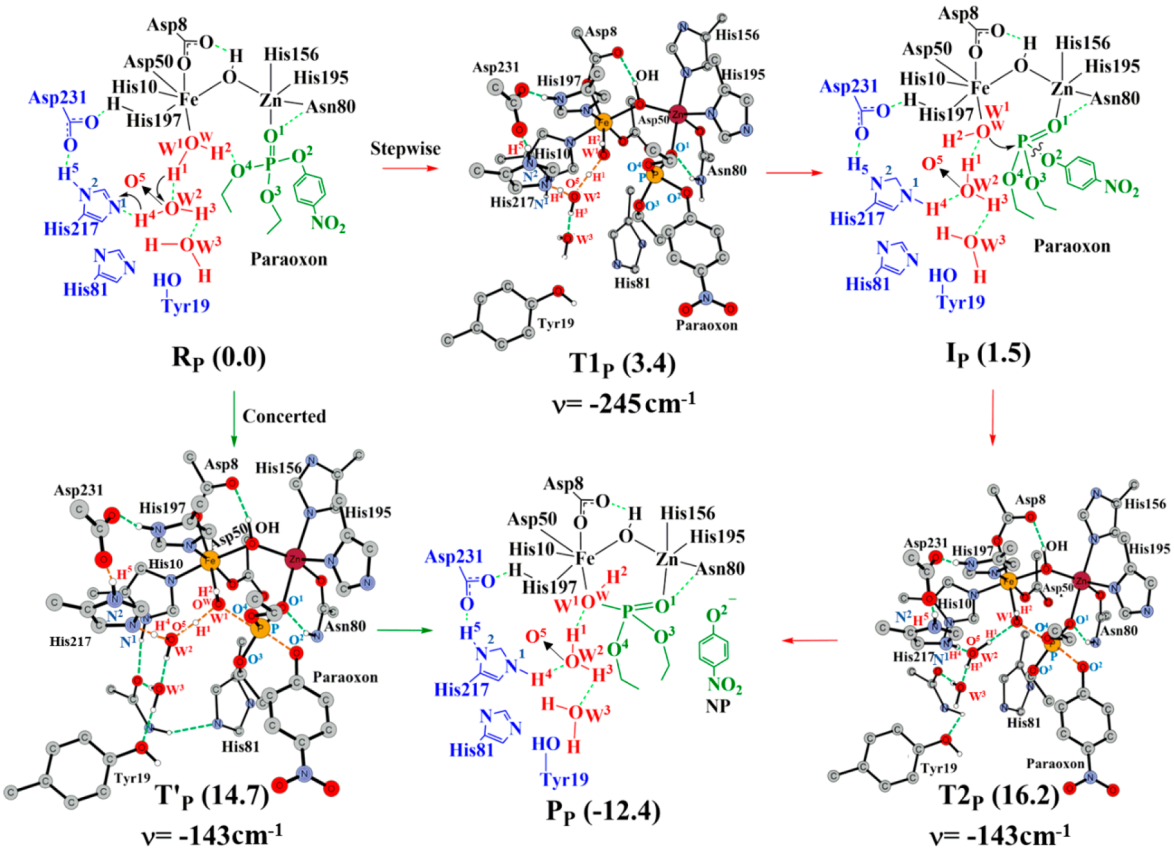

Figure 6. Structures (Å) and energies (kcal/mol) of the stepwise (red arrows) and concerted (green arrows) mechanisms for the paraoxon hydrolysis.

the noncleaved nitrophenyl group of BNPP (compare Figures 4 and 5).[35,63] Also similar to the GpdQ-BNPP complex the metal ions in the active site are only bridged by a μ-OH while Asp50 coordinates terminally to Fe(II) (the Fe−Zn distance in the most stable reactant $\mathbf{R}_N$ is 3.61 Å; Table 3). Interestingly, in $\mathbf{R}_N$ the only cleavable bond, P−O^2, is considerably longer (and thus weaker) than the corresponding bonds in the GPE and BNPP complexes (1.83 Å vs 1.70 and 1.72 Å, respectively), while the charges on the relevant reactants (the electrophilic P and nucleophilic O^W) are smaller (the charge differences e(P) − e(O^W) in $\mathbf{R}_G$, $\mathbf{R}_B$, and $\mathbf{R}_N$ are 3.45e, 3.45e, and 3.34e, respectively).

3.3.1. Stepwise Mechanism. The first step in the stepwise mechanism with NPP is very similar to its counterparts in the reactions with the diester substrates; the activation of W^1 by the base His217 occurs with a very low energy barrier and is nearly thermoneutral (Figure 5). In the intermediate ($\mathbf{I}_N$) formed in this step, in comparison to $\mathbf{I}_G$ and $\mathbf{I}_B$, the charge on the Fe atom is smaller by 0.06e and the Fe−O^W bond is substantially shorter by ∼0.11 Å (Tables 1−3). However, the P−O^2 bond is significantly longer by 0.12 Å than the corresponding bonds in both $\mathbf{I}_G$ and $\mathbf{I}_B$.

In the next step, consistent with the mechanisms discussed above, an attack by the Fe-bound O^W nucleophile triggers the cleavage of the P−O^2 bond. However, in contrast to the reactions with the diester substrates, here bond cleavage is linked to a proton transfer from His217 to the O^3 atom of NPP via W^2 (Figure 5). Here, a high negative charge on O^4 (−1.12e) and a positive charge on His217 promotes this transfer. In the optimized transition state ($\mathbf{T2}_N$), the sum of P−O^W and P−O^2 (4.22 Å; Table 3) indicates a lower degree of association than in the reaction with BNPP (4.04 Å), and the activation barrier is considerably larger (24 kcal/mol vs ∼10 kcal/mol). A higher barrier for this step is caused by the attack of the hydroxide (−O^WH^{2-}) on the negatively charged phosphate group of the substrate. Additionally, the P atom in $\mathbf{I}_N$ contains the lowest charge and it is the least electrophilic among all four substrates (Table 3). The calculated, rate-limiting activation barrier for NPP is in good agreement with the barrier reported for the NPP cleavage by another metallohydrolase, phospholipase C (23.8 kcal/mol),[85] and also with the considerably lower catalytic rate reported for this substrate.[18,40] The product state $\mathbf{P}_N$ lies, energetically (−16.0 kcal/mol), between its counterparts from the reaction with BNPP (−19.2 kcal/mol) and GPE (−13.5 kcal/mol). Two hydrogen bonds, one between O^3 and W^2 and a bifurcated bond between the product nitrophenol (NP) and Tyr19/W^2, add to the stability of $\mathbf{P}_N$ (Figure 5).

3.3.2. Concerted Mechanism. The major difference between NPP and the diester substrates in this concerted mechanism model is that His217 does not participate in the reaction with the monoester substrate. Instead, the ultimate proton acceptor is O^3 in the phosphate group (Figure 5). This pathway, previously proposed for the GpdQ-mediated hydrolysis of NPP,[15] is plausible due to the significantly higher charge on the O^3 atom of NPP (−1.12e) in comparison to its counterparts in the diester substrates (i.e., −0.81e and −0.89e for BNPP and GPE, respectively). Its barrier is 23.8 kcal/mol, virtually indistinguishable from that of the stepwise mechanism model, and the optimized transition state ($\mathbf{T'}_N$) is

https://dx.doi.org/10.1021/acscatal.9b04847
ACS Catal. 2020, 10, 3684−3696

Table 4. Key Geometrical Bond Distances (Å) and NBO Charges (e) of the Optimized Structures for the Stepwise and Concerted Mechanisms of the Paraoxon Hydrolysis

	bond distance (Å)									NBO charge (e)		
	O^W-H^1	H^1-O^5	O^5-H^4	H^4-N^1	$Fe-O^W$	$Zn-O^1$	Fe−Zn	$P-O^2$	$P-O^W$	Fe	P	O^W
Stepwise Mechanism												
$\mathbf{R_P}$	0.98	1.34	1.04	1.56	2.10	2.24	3.62	1.73	2.87	0.54	2.58	−0.92
$\mathbf{T1_P}$	1.21	1.36	1.31	1.26	1.99	2.14	3.62	1.72	2.58	0.58	2.56	−0.94
$\mathbf{I_P}$	2.10	1.02	2.25	1.03	2.01	2.14	3.62	1.73	2.54	0.58	2.56	−1.04
$\mathbf{T2_P}$	2.09	0.98	1.49	1.08	2.17	2.12	3.64	1.95	2.03	0.63	2.54	−0.95
$\mathbf{P_P}$	1.98	0.98	1.47	1.09	2.18	2.12	3.60	3.66	1.60	0.62	2.57	−1.03
Concerted Mechanism												
$\mathbf{T'_P}$	1.25	1.26	1.17	1.30	2.27	2.25	3.64	1.96	2.04	0.58	2.54	−0.93

also negligibly more associative (4.17 Å vs 4.22 Å; Table 3). This increased tightness in the concerted mechanism follows a conserved trend for each of the substrates.

3.4. Mechanism of Paraoxon Hydrolysis. Paraoxon is a phosphotriester pesticide with one nitrophenol and two ethyl groups (Figure 1a). In the most stable GpdQ-paraoxon complex ($\mathbf{R_P}$) the nitrophenyl group of paraoxon is exposed to the solvent, while both hydrophobic ethyl groups are buried deep inside the active site (Figure 6 and Figure S10).[63] The phosphate group of this substrate forms hydrogen bonds with Asn80 and W^1, but in contrast to the complexes with the mono- and diester substrates, no other residues in the active site make contacts. The metal centers are bridged only by the μ-OH, with Asp50 being coordinated monodentately to the Fe(II). The *p*-nitrophenol leaving group is located *trans* to W^1, the nucleophile of the GpdQ-catalyzed reaction (Figure 6). Paraoxon binds more weakly than the other substrates, demonstrated by its longer distances for the $Fe-O^W$ (2.10 Å) and $Zn-O^1$ (2.24 Å) bonds (Tables 1−4). Furthermore, the scissile $P-O^2$ bond in the GpdQ-paraoxon complex is elongated by only 0.05 Å in comparison to its free form and thus is considerably shorter (and more stable) than its counterparts in the other substrate complexes.

3.4.1. Stepwise Mechanism. The first step in the mechanism involves the familiar role of His217 as the base that creates a nucleophile from W^1. The barrier of this initial step (3.4 kcal/mol) and the energy increase of the resulting intermediate ($\mathbf{I_P}$) are comparable to those of the reactions with the mono- and diester substrates. Additionally, key structural parameters such as $Fe-O^W$ and $P-O^2$ bonds and the charge on the Fe atom in $\mathbf{I_P}$ are more similar to $\mathbf{I_G}$ and $\mathbf{I_B}$ than to $\mathbf{I_N}$ (Tables 1−4).

In the subsequent step, the Fe(II)-bound O^WH^2 nucleophile splits the $P-O^2$ bond. Similar to the reactions with the other substrates analyzed, this process is rate-limiting, occurring with a barrier (∼15 kcal/mol) that is substantially higher than that for the reaction with the diester substrates (<10 kcal/mol) but significantly smaller than that for the monoester substrate (>20 kcal/mol). This increase in the barrier is due to the extra stability of the $P-O^2$ bond of paraoxon in comparison to BNPP. This trend is in agreement with the experimentally determined preference of GpdQ for diesters, followed by tri- and monoester substrates.[15,40,59,86] In the optimized transition state ($\mathbf{T2_P}$), the sum of $P-O^W$ and $P-O^2$ bond distances (3.98 Å) is smaller than those of its counterparts in the reactions with BNPP (4.04 Å), GPE (4.19 Å), and NPP (4.22 Å), in agreement with experimental data that demonstrate the tightness of this transition state follows the trend paraoxon (triester) > BNPP (diester) > NPP (monoester).[43,44,87] Thus, the hydrolysis of the $P-O^2$ bond in paraoxon takes place via the $D_N + A_N$ mechanism: i.e., the nucleophile−electrophile ($P-O^W$) bond is stronger than the electrophile−leaving group ($P-O^2$) bond. The experimentally proposed shift toward this dissociative mechanism[44] is clearly reproduced in our calculations. The product state ($\mathbf{P_P}$) is the least exergonic state but is similar to that of the reaction with GPE (Figures 3 and 6); in both reactions only one hydrogen bond between the enzyme and product molecules is observed (between Asn80 and O^1, universally present in each of the reactions investigated; extra hydrogen bonds stabilize the product state in the reactions with BNPP and NPP, as discussed above).

3.4.2. Concerted Mechanism. Similar to the reaction with GPE, we investigated an alternative scenario whereby the formation of the O^WH^2 nucleophile and the concomitant attack on the P atom occur concertedly (step 1), before the scissile $P-O^2$ bond is cleaved (step 2; Figure S11 and Table S4). In comparison, only the nucleophile is created in the first step of the previous mechanism (Figure 6). In the intermediate ($\mathbf{I''_P}$ in Figure S11), the $-O^WH^2$ group is already bound to the P atom, whereas it is still coordinated to Fe in $\mathbf{I_P}$.

In contrast to the reaction with GPE, the energetics of the reaction with paraoxon is more favorable. The barriers for the two steps are 15.5 kcal/mol ($\mathbf{T1''_P}$) and 9.3 kcal/mol ($\mathbf{T2''_P}$). In comparison, in the stepwise mechanism described above and in Figure 6 the corresponding barriers are 3.4 kcal/mol ($\mathbf{T1_P}$) and 14.7 kcal/mol ($\mathbf{T2_P}$). The preferred mechanism thus cannot easily be distinguished from this comparison, and since the product state in the alternative mechanism is considerably more stable than that in the stepwise mechanism (−15.4 kcal vs −12.4 kcal/mol) the former seems more plausible.

We also investigated the concerted mechanism model (Figure 6). In this mechanism, the formation of the $\mathbf{I_P}$ intermediate is avoided and the $\mathbf{R_P} \rightarrow \mathbf{P_P}$ transformation takes place in a single step (Figure 6). The transition state ($\mathbf{T'_P}$) has a barrier (14.7 kcal/mol) that is very similar to those obtained from the other two models. Since there is no significant difference in the energy profiles of the three models described, and to facilitate a comparison between the reactions with GPE and paraoxon, we used the latter model to probe the cleavage of the ethanolate ester bond ($P-O^3$) in paraoxon (Figure S7 and Table S5). The cleavage of this bond occurs with a 2.6 kcal/mol higher barrier (Figure 6, Figure S7, Table 4, and Table S5). This difference is likely to be caused by the extra stabilization of $\mathbf{T'_P}$ in comparison to the transition state ($\mathbf{T_{PA}}$) in this case. From the corresponding reactant, the number of hydrogen bonds in $\mathbf{T_{PA}}$ remains the same (four bonds), while there is a gain of a hydrogen bond in $\mathbf{T'_P}$ (five

https://dx.doi.org/10.1021/acscatal.9b04847
ACS Catal. 2020, 10, 3684−3696

hydrogen bonds). The P−O^W and P−O^2 bond distances in T_{PA} are also shorter by 0.01 and 0.10 Å, respectively, than the distances in T'_P. These results show that there is a clear energetic preference for the cleavage of the P−O^2 over the P−O^3 bond. In contrast to GPE and BNPP substrates, paraoxon prefers the more dissociative mechanism and the transition state in the rate-limiting step of the mechanism is tighter than the transition states for the other two substrates.

4. CONCLUSIONS

In this DFT study, the chemical promiscuity of GpdQ has been investigated using four distinct phosphoester substrates, i.e. GPE and BNPP (both phosphodiesters), NPP (a phosphomonoester), and paraoxon (a phosphotriester), through three distinct mechanisms (stepwise, concerted, and substrate assisted). Among these mechanisms, both the stepwise and concerted mechanisms are the most favorable and occur with comparable barriers for all four substrates. The potential energy surface diagrams for these mechanisms are shown in Figure 7. Our results suggest that, among Tyr19, His81, and

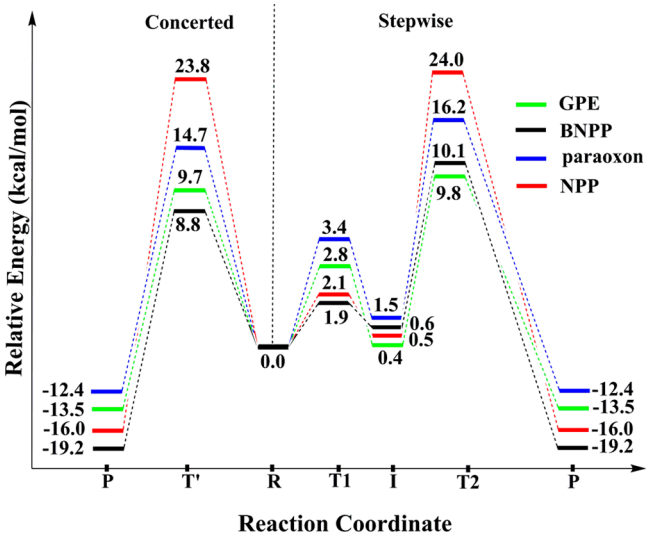

Figure 7. Potential energy surface (PES) diagrams for the stepwise and concerted mechanisms for the GPE, BNPP, paraoxon, and NPP substrates.

His217, the last residue is the most likely catalytic acid/base residue. Its significance in the mechanism of GpdQ was illustrated through structural, spectroscopic, and site-directed mutagenesis studies[12,23] and similar studies with the equivalent histidine residue in related metallohydrolases such as PAP,[12] RNaseZ,[80] and phosphoprotein phosphatases.[81] Among the two scissile bonds of GPE, hydrolysis of the glycerolate bond is more feasible than cleavage of the aminoethanolate bond. Furthermore, while the two diesters GPE and BNPP are hydrolyzed by GpdQ with similar energetics, the transition state in the rate-limiting step for GPE is looser than the corresponding transition state for BNPP, and the hydrolysis of the former occurs via a less associative mechanism. On the other hand, the monoester NPP utilizes a different type of stepwise mechanism that is also less associative than the mechanism used by all other substrates. On the other extreme of the substrate spectrum, the triester paraoxon favors a more dissociative mechanism and the transition state in the rate-determining step of its hydrolysis is also tighter. Among the two available phosphoester bonds of this substrate (*p*-nitrophenolate and ethanolate), hydrolysis of the former is energetically more favorable. The computed energetics demonstrate that the enzyme displays higher activity toward GPE and BNPP, followed by paraoxon and NPP. This order of activity, i.e. diesterase > triesterase > monoesterase, is in excellent agreement with experiments.[15] In summary, GpdQ is one of the most promiscuous phosphatases/metallohydrolases known to date, and this paper describes the first systematic comparison of the mechanism employed for the hydrolysis of diverse substrates (i.e., mono-, di-, and triesters). In addition to advancing our conceptual understanding of important factors that underpin the mechanism of GpdQ, the excellent agreement between computational and experimental data also provides a reliable methodology for the practical enhancement of the properties of a catalyst that has attracted significant interest in the biotechnology sector (as a bioremediator of pesticide-polluted environments and as an antiwarfare agent).

■ ASSOCIATED CONTENT

Supporting Information

The Supporting Information is available free of charge at https://pubs.acs.org/doi/10.1021/acscatal.9b04847.

Figures S1−S12 and Tables S1−S5 as described in the text, details of the substrate-assisted mechanism for GPE hydrolysis, and molecular dynamics (MD) simulations and Cartesian coordinates of all optimized structures (PDF)

■ AUTHOR INFORMATION

Corresponding Author

Rajeev Prabhakar − *Department of Chemistry, University of Miami, Coral Gables, Florida 33146, United States;* orcid.org/0000-0003-1137-1272; Phone: 305-284-9372; Email: rpr@miami.edu; Fax: 305-284-4571

Authors

Gaurav Sharma − *Department of Chemistry, University of Miami, Coral Gables, Florida 33146, United States*

Vindi M. Jayasinghe-Arachchige − *Department of Chemistry, University of Miami, Coral Gables, Florida 33146, United States*

Qiaoyu Hu − *Department of Chemistry, University of Miami, Coral Gables, Florida 33146, United States*

Gerhard Schenk − *School of Chemistry and Molecular Biosciences, The University of Queensland, St. Lucia, Queensland 4072, Australia*

Complete contact information is available at: https://pubs.acs.org/10.1021/acscatal.9b04847

Notes

The authors declare no competing financial interest.

■ ACKNOWLEDGMENTS

The authors declare no competing financial interests. This material is based upon work supported by a grant from the National Science Foundation (Grant Number CHE-1664926) to R.P. Computational resources from the Center for Computational Science (CCS) at the University of Miami to R.P. are also greatly appreciated.

https://dx.doi.org/10.1021/acscatal.9b04847
ACS Catal. 2020, 10, 3684−3696

REFERENCES

(1) Gerlt, J. A.; Westheimer, F. H. Phosphodiesterase from Enterobacter aerogenes. *J. Am. Chem. Soc.* **1973**, *95*, 8166−8168.
(2) Gerlt, J. A.; Whitman, G. J. Purification and properties of a phosphohydrolase from *Enterobacter aerogenes*. *J. Biol. Chem.* **1975**, *250*, 5053−5058.
(3) Kaija, H.; Alatalo, S. L.; Halleen, J. M.; Lindqvist, Y.; Schneider, G.; Väänänen, H. K.; Vihko, P. Phosphatase and Oxygen Radical-Generating Activities of Mammalian Purple Acid Phosphatase Are Functionally Independent. *Biochem. Biophys. Res. Commun.* **2002**, *292*, 128−132.
(4) Räisänen, S. R.; Alatalo, S. L.; Ylipahkala, H.; Halleen, J. M.; Cassady, A. I.; Hume, D. A.; Väänänen, H. K. Macrophages overexpressing tartrate-resistant acid phosphatase show altered profile of free radical production and enhanced capacity of bacterial killing. *Biochem. Biophys. Res. Commun.* **2005**, *331*, 120−126.
(5) Oddie, G. W.; Schenk, G.; Angel, N. Z.; Walsh, N.; Guddat, L. W.; de Jersey, J.; Cassady, A. I.; Hamilton, S. E.; Hume, D. A. Structure, function, and regulation of tartrate-resistant acid phosphatase. *Bone* **2000**, *27*, 575−584.
(6) Nuttleman, P.; Roberts, M. Transfer of Iron from Uteroferrin (Purple Acid Phosphatase) to Transferrin Related to Acid Phosphatase Activity. *J. Biol. Chem.* **1990**, *265*, 12192−12199.
(7) Mitić, N.; Smith, S. J.; Neves, A.; Guddat, L. W.; Gahan, L. R.; Schenk, G. The Catalytic Mechanisms of Binuclear Metallohydrolases. *Chem. Rev.* **2006**, *106*, 3338−3363.
(8) Jackson, M. D.; Denu, J. M. Molecular Reactions of Protein Phosphatases: Insights from Structure and Chemistry. *Chem. Rev.* **2001**, *101*, 2313−2340.
(9) Wilcox, D. E. Binuclear Metallohydrolases. *Chem. Rev.* **1996**, *96*, 2435−2458.
(10) Lowther, W. T.; Matthews, B. W. Metalloaminopeptidases: Common Functional Themes in Disparate Structural Surroundings. *Chem. Rev.* **2002**, *102*, 4581−4608.
(11) Crowder, M. W.; Spencer, J.; Vila, A. J. Metallo-β-lactamases: novel weaponry for antibiotic resistance in bacteria. *Acc. Chem. Res.* **2006**, *39*, 721−728.
(12) Daumann, L. J.; McCarthy, B. Y.; Hadler, K. S.; Murray, T. P.; Gahan, L. R.; Larrabee, J. A.; Ollis, D. L.; Schenk, G. *Biochim. Biophys. Acta, Proteins Proteomics* **2013**, *1834*, 425−432.
(13) Hadler, K. S.; Mitić, N.; Ely, F.; Hanson, G. R.; Gahan, L. R.; Larrabee, J. A.; Ollis, D. L.; Schenk, G. Structural Flexibility Enhances the Reactivity of the Bioremediator Glycerophosphodiesterase by Fine-Tuning Its Mechanism of Hydrolysis. *J. Am. Chem. Soc.* **2009**, *131*, 11900−11908.
(14) Schenk, G.; Mateen, I.; Ng, T.-K.; Pedroso, M. M.; Mitić, N.; Jafelicci, M.; Marques, R. F. C.; Gahan, L. R.; Ollis, D. L. Organophosphate-degrading metallohydrolases: Structure and function of potent catalysts for applications in bioremediation. *Coord. Chem. Rev.* **2016**, *317*, 122−131.
(15) Ghanem, E.; Li, Y.; Xu, C.; Raushel, F. M. Characterization of a Phosphodiesterase Capable of Hydrolyzing EA 2192, the Most Toxic Degradation Product of the Nerve Agent VX±. *Biochemistry* **2007**, *46*, 9032−9040.
(16) Ghanem, E.; Raushel, F. M. Detoxification of organophosphate nerve agents by bacterial phosphotriesterase. *Toxicol. Appl. Pharmacol.* **2005**, *207*, 459−470.
(17) Daumann, L. J.; Larrabee, J. A.; Ollis, D.; Schenk, G.; Gahan, L. R. Immobilization of the enzyme GpdQ on magnetite nanoparticles for organophosphate pesticide bioremediation. *J. Inorg. Biochem.* **2014**, *131*, 1−7.
(18) Hadler, K. S.; Tanifum, E. A.; Yip, S. H.-C.; Mitic, N.; Guddat, L. W.; Jackson, C. J.; Gahan, L. R.; Nguyen, K.; Carr, P. D.; Ollis, D. L. Substrate-promoted formation of a catalytically competent binuclear center and regulation of reactivity in a glycerophosphodiesterase from *Enterobacter aerogenes*. *J. Am. Chem. Soc.* **2008**, *130*, 14129−14138.
(19) Schenk, G.; Neidig, M. L.; Zhou, J.; Holman, T. R.; Solomon, E. I. Spectroscopic Characterization of Soybean Lipoxygenase-1 Mutants: the Role of Second Coordination Sphere Residues in the Regulation of Enzyme Activity±. *Biochemistry* **2003**, *42*, 7294−7302.
(20) Neidig, M. L.; Wecksler, A. T.; Schenk, G.; Holman, T. R.; Solomon, E. I. Kinetic and Spectroscopic Studies of N694C Lipoxygenase: A Probe of the Substrate Activation Mechanism of a Nonheme Ferric Enzyme. *J. Am. Chem. Soc.* **2007**, *129*, 7531−7537.
(21) Mullen, G. P.; Serpersu, E. H.; Ferrin, L. J.; Loeb, L. A.; Mildvan, A. S. Metal binding to DNA polymerase I, its large fragment, and two 3′, 5′-exonuclease mutants of the large fragment. *J. Biol. Chem.* **1990**, *265*, 14327−14334.
(22) Hadler, K. S.; Mitić, N.; Yip, S. H.-C.; Gahan, L. R.; Ollis, D. L.; Schenk, G.; Larrabee, J. A. ElectronicStructure Analysis of the Dinuclear Metal Center in the Bioremediator Glycerophosphodiesterase (GpdQ) from *Enterobacter aerogenes*. *Inorg. Chem.* **2010**, *49*, 2727−2734.
(23) Jackson, C. J.; Hadler, K. S.; Carr, P. D.; Oakley, A. J.; Yip, S.; Schenk, G.; Ollis, D. L. Malonate-bound structure of the glycerophosphodiesterase from *Enterobacter aerogenes* (GpdQ) and characterization of the native Fe^{2+} metal-ion preference. *Acta Crystallogr., Sect. F: Struct. Biol. Cryst. Commun.* **2008**, *64*, 681−685.
(24) Schenk, G.; Mitić, N.; Hanson, G. R.; Comba, P. Purple acid phosphatase: A journey into the function and mechanism of a colorful enzyme. *Coord. Chem. Rev.* **2013**, *257*, 473−482.
(25) Mitić, N.; Miraula, M.; Selleck, C.; Hadler, K. S.; Uribe, E.; Pedroso, M. M.; Schenk, G.; Christov, C. Z. Catalytic Mechanisms of Metallohydrolases Containing Two Metal Ions. *Adv. Protein Chem. Struct. Biol.* **2014**, *97*, 49−81.
(26) Jackson, C. J.; Carr, P. D.; Liu, J.-W.; Watt, S. J.; Beck, J. L.; Ollis, D. L. The Structure and Function of a Novel Glycerophosphodiesterase from *Enterobacter aerogenes*. *J. Mol. Biol.* **2007**, *367*, 1047−1062.
(27) Pedroso, M. M.; Larrabee, J. A.; Ely, F.; Gwee, S. E.; Mitić, N.; Ollis, D. L.; Gahan, L. R.; Schenk, G. Ca^{II} Binding Regulates and Dominates the Reactivity of a Transition-Metal-Ion-Dependent Diesterase from *Mycobacterium tuberculosis*. *Chem. - Eur. J.* **2016**, *22*, 999−1009.
(28) Lowther, W. T.; Matthews, B. W. Structure and function of the methionine aminopeptidases. *Biochim. Biophys. Acta, Protein Struct. Mol. Enzymol.* **2000**, *1477*, 157−167.
(29) Mirams, R. E.; Smith, S. J.; Hadler, K. S.; Ollis, D. L.; Schenk, G.; Gahan, L. R. Cadmium(II) complexes of the glycerophosphodiester-degrading enzyme GpdQ and a biomimetic N,O ligand. *JBIC, J. Biol. Inorg. Chem.* **2008**, *13*, 1065−1072.
(30) Aubert, S. D.; Li, Y.; Raushel, F. M. Mechanism for the Hydrolysis of Organophosphates by the Bacterial Phosphotriesterase ±. *Biochemistry* **2004**, *43*, 5707−5715.
(31) Ely, F.; Hadler, K.; Gahan, L.; Guddat, L.; Ollis, D.; Schenk, G. The organophosphate-degrading enzyme from *Agrobacterium radiobacter* displays mechanistic flexibility for catalysis. *Biochem. J.* **2010**, *432*, 565−573.
(32) Zambelli, B.; Musiani, F.; Benini, S.; Ciurli, S. Chemistry of Ni^{2+} in Urease: Sensing, Trafficking, and Catalysis. *Acc. Chem. Res.* **2011**, *44*, 520−530.
(33) McGeary, R. P.; Schenk, G.; Guddat, L. W. The applications of binuclear metallohydrolases in medicine: Recent advances in the design and development of novel drug leads for purple acid phosphatases, metallo-β-lactamases and arginases. *Eur. J. Med. Chem.* **2014**, *76*, 132−144.
(34) Mitic, N.; Hadler, K. S.; Gahan, L. R.; Hengge, A. C.; Schenk, G. The divalent metal ion in the active site of uteroferrin modulates substrate binding and catalysis. *J. Am. Chem. Soc.* **2010**, *132*, 7049−7054.
(35) Paul, T. J.; Schenk, G.; Prabhakar, R. Formation of Catalytically Active Binuclear Center of Glycerophosphodiesterase: A Molecular Dynamics Study. *J. Phys. Chem. B* **2018**, *122*, 5797−5808.
(36) Pedroso, M. M.; Ely, F.; Carpenter, M. C.; Mitić, N. a.; Gahan, L. R.; Ollis, D. L.; Wilcox, D. E.; Schenk, G. Mechanistic Insight from Calorimetric Measurements of the Assembly of the Binuclear Metal

https://dx.doi.org/10.1021/acscatal.9b04847
ACS Catal. 2020, 10, 3684−3696

Active Site of Glycerophosphodiesterase (GpdQ) from *Enterobacter aerogenes*. *Biochemistry* **2017**, *56*, 3328−3336.
(37) Jackson, C. J.; Carr, P. D.; Kim, H.-K.; Liu, J.-W.; Herrald, P.; Mitić, N.; Schenk, G.; Smith, C. A.; Ollis, D. L. Anomalous scattering analysis of *Agrobacterium radiobacter* phosphotriesterase: the prominent role of iron in the heterobinuclear active site. *Biochem. J.* **2006**, *397*, 501−508.
(38) Ely, F.; Hadler, K. S.; Mitić, N.; Gahan, L. R.; Ollis, D. L.; Plugis, N. M.; Russo, M. T.; Larrabee, J. A.; Schenk, G. Electronic and geometric structures of the organophosphate-degrading enzyme from *Agrobacterium radiobacter* (OpdA). *JBIC, J. Biol. Inorg. Chem.* **2011**, *16*, 777−787.
(39) Cox, R. S.; Schenk, G.; Mitić, N.; Gahan, L. R.; Hengge, A. C. Diesterase activity and substrate binding in purple acid phosphatases. *J. Am. Chem. Soc.* **2007**, *129*, 9550−9551.
(40) Hadler, K. S.; Gahan, L. R.; Ollis, D. L.; Schenk, G. The bioremediator glycerophosphodiesterase employs a non-processive mechanism for hydrolysis. *J. Inorg. Biochem.* **2010**, *104*, 211−213.
(41) O'Ferrall, R. M. Relationships between E2 and E1cB mechanisms of β-elimination. *J. Chem. Soc. B* **1970**, *0*, 274−277.
(42) Kirby, A. J.; Nome, F. Fundamentals of phosphate transfer. *Acc. Chem. Res.* **2015**, *48*, 1806−1814.
(43) Cassano, A. G.; Anderson, V. E.; Harris, M. E. Understanding the transition states of phosphodiester bond cleavage: Insights from heavy atom isotope effects. *Biopolymers* **2004**, *73*, 110−129.
(44) Lassila, J. K.; Zalatan, J. G.; Herschlag, D. Biological phosphoryl-transfer reactions: understanding mechanism and catalysis. *Annu. Rev. Biochem.* **2011**, *80*, 669−702.
(45) Duarte, F.; Åqvist, J.; Williams, N. H.; Kamerlin, S. C. Resolving apparent conflicts between theoretical and experimental models of phosphate monoester hydrolysis. *J. Am. Chem. Soc.* **2015**, *137*, 1081−1093.
(46) Alberto, M. E.; Pinto, G.; Russo, N.; Toscano, M. Triesterase and Promiscuous Diesterase Activities of a Di-Co^{II}-Containing Organophosphate Degrading Enzyme Reaction Mechanisms. *Chem. - Eur. J.* **2015**, *21*, 3736−3745.
(47) López-Canut, V.; Roca, M.; Bertrán, J.; Moliner, V.; Tuñón, I. Theoretical study of phosphodiester hydrolysis in nucleotide pyrophosphatase/phosphodiesterase. Environmental effects on the reaction mechanism. *J. Am. Chem. Soc.* **2010**, *132*, 6955−6963.
(48) Klähn, M.; Rosta, E.; Warshel, A. On the mechanism of hydrolysis of phosphate monoesters dianions in solutions and proteins. *J. Am. Chem. Soc.* **2006**, *128*, 15310−15323.
(49) Bigley, A. N.; Raushel, F. M. Catalytic mechanisms for phosphotriesterases. *Biochim. Biophys. Acta, Proteins Proteomics* **2013**, *1834*, 443−453.
(50) Klabunde, T.; Sträter, N.; Fröhlich, R.; Witzel, H.; Krebs, B. Mechanism of Fe (III)-Zn (II) purple acid phosphatase based on crystal structures. *J. Mol. Biol.* **1996**, *259*, 737−748.
(51) Chen, S. L.; Liao, R. Z. Phosphate monoester hydrolysis by trinuclear alkaline phosphatase; DFT study of transition states and reaction mechanism. *ChemPhysChem* **2014**, *15*, 2321−2330.
(52) Borosky, G. L. Quantum-Mechanical Study on the Catalytic Mechanism of Alkaline Phosphatases. *J. Chem. Inf. Model.* **2017**, *57*, 540−549.
(53) Borosky, G. L. Catalytic activity of human placental alkaline phosphatase (PLAP): Insights from a computational study. *J. Phys. Chem. B* **2014**, *118*, 14302−14313.
(54) Kamerlin, S. C. L. Theoretical comparison of p-nitrophenyl phosphate and sulfate hydrolysis in aqueous solution: implications for enzyme-catalyzed sulfuryl transfer. *J. Org. Chem.* **2011**, *76*, 9228−9238.
(55) Zhang, H.; Yang, L.; Yan, L.-F.; Liao, R.-Z.; Tian, W.-Q. Evolution of phosphotriesterase activities of the metallo-β-lactamase family: A theoretical study. *J. Inorg. Biochem.* **2018**, *184*, 8−14.
(56) Zhang, H.; Yang, L.; Ding, W.; Ma, Y. The pH-dependent activation mechanism of Ser102 in Escherichia coli alkaline phosphatase: a theoretical study. *JBIC, J. Biol. Inorg. Chem.* **2018**, *23*, 277−284.
(57) Schenk, G.; Mitić, N. a.; Gahan, L. R.; Ollis, D. L.; McGeary, R. P.; Guddat, L. W. Binuclear metallohydrolases: Complex mechanistic strategies for a simple chemical reaction. *Acc. Chem. Res.* **2012**, *45*, 1593−1603.
(58) Roston, D.; Cui, Q. Substrate and transition state binding in alkaline phosphatase analyzed by computation of oxygen isotope effects. *J. Am. Chem. Soc.* **2016**, *138*, 11946−11957.
(59) Daumann, L. J.; Schenk, G.; Ollis, D. L.; Gahan, L. R. Spectroscopic and mechanistic studies of dinuclear metallohydrolases and their biomimetic complexes. *Dalton Trans.* **2014**, *43*, 910−928.
(60) Case, D. A.; Cheatham III, T. E.; Darden, T.; Gohlke, H.; Luo, R.; Merz, K. M., Jr; Onufriev, A.; Simmerling, C.; Wang, B.; Woods, R. J. The Amber Biomolecular Simulation Programs. *J. Comput. Chem.* **2005**, *26*, 1668−1688.
(61) Ren, P.; Wu, C.; Ponder, J. W. Polarizable Atomic Multipole-Based Molecular Mechanics for Organic Molecules. *J. Chem. Theory Comput.* **2011**, *7*, 3143−3161.
(62) Shi, Y.; Xia, Z.; Zhang, J.; Best, R.; Wu, C.; Ponder, J. W.; Ren, P. Polarizable Atomic Multipole-Based AMOEBA Force Field for Proteins. *J. Chem. Theory Comput.* **2013**, *9*, 4046−4063.
(63) Sharma, G.; Hu, Q.; Jayasinghe-Arachchige, V.; Paul, T.; Schenk, G.; Prabhakar, R. Investigating Coordination Flexibility of Glycerophosphodiesterase (GpdQ) Through Interactions with Mono-, Di-, and Triphosphoester (NPP, BNPP, GPE, and Paraoxon) Substrates. *Phys. Chem. Chem. Phys.* **2019**, *21*, 5499−5509.
(64) Kim, S.; Thiessen, P. A.; Bolton, E. E.; Chen, J.; Fu, G.; Gindulyte, A.; Han, L.; He, J.; He, S.; Shoemaker, B. A. PubChem Substance and Compound databases. *Nucleic Acids Res.* **2016**, *44*, D1202−D1213.
(65) Adamo, C.; Barone, V. Exchange functionals with improved long-range behavior and adiabatic connection methods without adjustable parameters: The mPW and m PW1PW models. *J. Chem. Phys.* **1998**, *108*, 664−675.
(66) Frisch, M.; Trucks, G.; Schlegel, H.; Scuseria, G.; Robb, M.; Cheeseman, J.; Scalmani, G.; Barone, V.; Mennucci, B.; Petersson, G., et al. *Gaussian 09, rev. D.01*; Gaussian, Inc.: Wallingford, CT, 2009.
(67) Hay, P. J.; Wadt, W. R. Ab initio effective core potentials for molecular calculations. Potentials for the transition metal atoms Sc to Hg. *J. Chem. Phys.* **1985**, *82*, 270−283.
(68) Cances, E.; Mennucci, B.; Tomasi, J. A new integral equation formalism for the polarizable continuum model: Theoretical background and applications to isotropic and anisotropic dielectrics. *J. Chem. Phys.* **1997**, *107*, 3032−3041.
(69) Schuchardt, K. L.; Didier, B. T.; Elsethagen, T.; Sun, L.; Gurumoorthi, V.; Chase, J.; Li, J.; Windus, T. L. Basis set exchange: a community database for computational sciences. *J. Chem. Inf. Model.* **2007**, *47*, 1045−1052.
(70) Zhao, Y.; Truhlar, D. G. The M06 suite of density functionals for main group thermochemistry, thermochemical kinetics, noncovalent interactions, excited states, and transition elements: two new functionals and systematic testing of four M06-class functionals and 12 other functionals. *Theor. Chem. Acc.* **2008**, *120*, 215−241.
(71) Becke, A. D. Density-functional exchange-energy approximation with correct asymptotic behavior. *Phys. Rev. A: At., Mol., Opt. Phys.* **1988**, *38*, 3098−3100.
(72) Becke, A. D. Density-functional thermochemistry:III. The role of extract exchange. *J. Chem. Phys.* **1993**, *98*, 5648−5652.
(73) Perdew, J. P.; Burke, K.; Ernzerhof, M. Generalized gradient approximation made simple. *Phys. Rev. Lett.* **1996**, *77*, 3865−3868.
(74) Sosa, C.; Andzelm, J.; Elkin, B. C.; Wimmer, E.; Dobbs, K. D.; Dixon, D. A. A local density functional study of the structure and vibrational frequencies of molecular transition-metal compounds. *J. Phys. Chem.* **1992**, *96*, 6630−6636.
(75) Hay, P.; Dunning, T., Jr. *Modern Theoretical Chemistry*; Schaefer, H. F., III, Ed.; Plenum: New York, 1976; Vol. 3 (Methods of Electronic Structure Theory).
(76) Grimme, S.; Ehrlich, S.; Goerigk, L. Effect of the damping function in dispersion corrected density functional theory. *J. Comput. Chem.* **2011**, *32*, 1456−1465.

https://dx.doi.org/10.1021/acscatal.9b04847
ACS Catal. 2020, 10, 3684−3696

(77) Prince, R.; Woolley, P. Metal ion function in carbonic anhydrase. *Angew. Chem., Int. Ed. Engl.* **1972**, *11*, 408−417.
(78) Groves, J. T.; Olson, J. R. Models of zinc-containing proteases. Rapid amide hydrolysis by an unusually acidic Zn^{2+}-OH_2 complex. *Inorg. Chem.* **1985**, *24*, 2715−2717.
(79) Alberto, M. E.; Marino, T.; Ramos, M. J.; Russo, N. Atomistic details of the Catalytic Mechanism of Fe(III)- Zn(II) Purple Acid Phosphatase. *J. Chem. Theory Comput.* **2010**, *6*, 2424−2433.
(80) Liao, R. Z.; Himo, F.; Yu, J. G.; Liu, R. Z. Theoretical study of the RNA hydrolysis mechanism of the dinuclear zinc enzyme RNase Z. *Eur. J. Inorg. Chem.* **2009**, *2009*, 2967−2972.
(81) Zhang, H.; Ma, Y.; Yu, J.-G. Theoretical studies on the mechanism of activation of phosphoprotein phosphatases and purple acid phosphatases suggest an evolutionary strategy to survive in acidic environments. *JBIC, J. Biol. Inorg. Chem.* **2013**, *18*, 1019−1026.
(82) Marie-Claire, C.; Ruffet, E.; Antonczak, S.; Beaumont, A.; O'Donohue, M.; Roques, B. P.; Fournié-Zaluski, M.-C. Evidence by site-directed mutagenesis that arginine 203 of thermolysin and arginine 717 of neprilysin (neutral endopeptidase) play equivalent critical roles in substrate hydrolysis and inhibitor binding. *Biochemistry* **1997**, *36*, 13938−13945.
(83) Pereira, E. S.; Da Silva, J. C.; Brandão, T. A.; Rocha, W. R. Phosphorane lifetime and stereo-electronic effects along the alkaline hydrolysis of phosphate esters. *Phys. Chem. Chem. Phys.* **2016**, *18*, 18255−18267.
(84) Mikkola, S.; Lönnberg, T.; Lönnberg, H. Phosphodiester models for cleavage of nucleic acids. *Beilstein J. Org. Chem.* **2018**, *14*, 803−837.
(85) Liao, R.-Z.; Yu, J.-G.; Himo, F. Reaction mechanism of the trinuclear zinc enzyme phospholipase C: A density functional theory study. *J. Phys. Chem. B* **2010**, *114*, 2533−2540.
(86) McLoughlin, S. Y.; Jackson, C.; Liu, J.-W.; Ollis, D. L. Growth of Escherichia coli Coexpressing Phosphotriesterase and Glycerophosphodiester Phosphodiesterase, Using Paraoxon as the Sole Phosphorus Source. *Appl. Environ. Microbiol.* **2004**, *70*, 404−412.
(87) Mancin, F.; Scrimin, P.; Tecilla, P. Progress in artificial metallonucleases. *Chem. Commun.* **2012**, *48*, 5545−5559.

https://dx.doi.org/10.1021/acscatal.9b04847
ACS Catal. 2020, 10, 3684−3696